Standardized Kalman Filtering for Time Serial Source Localization of Simultaneous Subcortical and Cortical Brain Activity

Standardized Kalman Filtering for Time Serial Source Localization of Simultaneous Subcortical and Cortical Brain Activity

Joonas Lahtinen ⬤, Paavo Ronni, Narayan Puthanmadam Subramaniyam, Alexandra Koulouri, Carsten Wolters, Sampsa Pursiainen

Abstract— In this article, we present a new Bayesian filtering method for non-invasive electroencephalography (EEG) that is capable of reconstructing spatiotemporal brain activity, including both cortical and weakly detectable deep components. Our approach improves upon the standard Bayesian recursive filtering method, also known as Kalman filtering, by introducing an additional step that re-weights the instantaneous reconstructions akin to the Standardized low-resolution brain electromagnetic tomography (sLORETA). This interim step helps to reduce any potential source depth biases, resulting in more accurate tracking of the dynamics of brain activity and better localization of dipolar components than distributed spatiotemporal Kalman filtering without any standardization or time-independent approaches, such as sLORETA. Our numerical simulations and reconstructions of real realistic somatosensory evoked potentials demonstrate that our proposed algorithmic framework can effectively track the time evolution and localize simultaneously both deep and superficial brain activity. Therefore, our method offers a promising solution for researchers and clinicians interested in investigating the dynamic behavior of brain activity.

Index Terms— Electroencephalography (EEG), Finite element method (FEM), Human head model, Inverse methods, Source Localization, Spatiotemporal

J. Lahtinen, P. Ronni, A. Koulouri, and S. Pursiainen are with Computing Sciences Unit, Faculty of Information Technology and Communication Sciences, Tampere University, 33720 Tampere, Finland (e-mail: joonas.j.lahtinen@tuni.fi; paavo.ronni@live.com; alexandra.koulouri@tuni.fi; smpsa.pursinen@tuni.fi).

N. P. Subramaniyam is with Faculty of Medicine and Health Technology, Tampere University, 33720 Tampere, Finland (e-mail: narayan.subramaniyam@tuni.fi).

C. Wolters is with Institute for Biomagnetism and Biosignalanalysis, University of Münster, 48149 Munster, Germany (e-mail: carsten.wolters@uni-muenster.de).

Corresponding author: Joonas Lahtinen

Color versions of one or more of the figures in this paper are available online at http://ieeexplore.ieee.org

I. INTRODUCTION

Electroencephalograph (EEG) is a standard non-invasive modality to record neuronal activity from the scalp surface with high temporal resolution [1]. EEG source imaging problem is the reconstruction of the brain activity using the EEG potential recordings [2]. This problem is severely ill-posed without a unique solution if no prior assumptions are given for brain activity. Nowadays, there are numerous inversion methods for source localization with diverse prior assumptions [3]. Only some of them take the temporal aspect of biopotential recordings into account in the modeling [4]–[8]. These methods employ spatiotemporal priors and aim to solve a large optimization problem. To reduce the computational effort of these large problems, a coarse source space is often used which results in deteriorating the spatial resolution of the source reconstruction [9].

An alternative path to capture the source activity course with high spatiotemporal resolution is to use Bayesian filtering. Considering linear Gaussian state-space modeling, this leads to the well-known Kalman filter (KF) [10]. Kalman filter has been previously used to reconstruct simulated and real brain activity distributions from EEG recordings using a regular grid-based low-resolution brain model [11], [12], and later coupled with LORETA method forming DynLORETA [13], where an approximation of the Kalman filter is used. It is also used to reconstruct cortical components of somatosensory evoked potentials from magnetoencephalography (MEG) recordings [14] and in combination with EEG/MEG in localization of epileptic spikes [15] using high-resolution models. The regional version of spatitemporal Kalman is obtained to localize deep brain activity correctly [16], where the nearest-neighbor coupling is used to simplify the computation. However, the fully-coupled state-space Kalman filtering approaches suffer from depth-biased estimations, meaning that it favors reconstructions in superficial brain locations while failing to recover deep activity, similarly to the well-known minimum norm estimate [17]. To overcome the depth bias of MNE, Standardized low-resolution brain electromagnetic tomography (sLORETA) has been developed [18]. The idea

is to modify the minimum norm estimation so that the estimated variables are standardized current densities, which were found to have high localization accuracy [19], [20] and high measurement noise robustness [21], [22].

In this work, we propose a standardized Kalman filtering. As the first step, we give a probability-based interpretation for sLORETA. Then, we introduce a novel sLORETA-type standardization to the dynamical EEG source imaging problem, namely to the Kalman filtering, where the state-space output of the Kalman filter is modified so that the estimated source reconstruction is standardized in order to reduce the depth bias. After that, we conduct experiments with synthetical and real non-invasive EEG recordings of somatosensory evoked potentials (SEP) showing the difference of spatial sLORETA, Kalman, and standardized Kalman filtering (SKF) estimation. We have selected SEP data because it is previously well-studied known originator locations [23]–[26]. We want to pinpoint that reconstruction of weak deep activity is a difficult task that has grown in interest in recent years [27].

In the result section, we demonstrate the difference of spatial sLORETA, Kalman, and standardized Kalman filtering (SKF) estimation. Our results show that the usage of the Kalman filter smooths the estimation while the standardization improves the localization. In effect, the combination of the standardization and dynamical filtering was found to improve the localization and ability to track dynamical changes in the system containing cortical and subcortical activity better than these approaches separately. Moreover, the subcortical components of SEP data are correctly localized only with a standardized Kalman filter. Finally, we test our algorithm with real SEP. Our findings reveal that SKF produces a more coherent and focal reconstruction of the underlying activity compared to the two other methods.

II. METHODS

A. Bioelectromagnetic Forward Problem

The purpose of the EEG forward model is to model the biosignals inside the brain when the primary current field $\mathbf{J}^P$ is given inside the brain. The quasi-static approximation of Maxwell's equations leads to the following Poisson's problem with isolation condition for the electric field as the boundary condition

$$\begin{aligned} \nabla \cdot (\sigma \nabla u) &= \nabla \cdot \mathbf{J}^P \quad \text{in } \Omega, \\ \mathbf{n} \cdot (\sigma \nabla u) &= 0 \quad\quad\ \text{on } \partial\Omega, \end{aligned} \quad (1)$$

where σ is a positive definite conductivity tensor, u denotes electric potentials, and $\mathbf{n}$ is the normal vector of the head model's boundary. In a FEM-based approach, the electrical potentials and current density field are approximated via a finite set of basis functions. In this study, the primary current field is approximated using H(div) basis functions [28]. This yields a linearized problem written here in time-varying form

$$\mathbf{y}_t = L\mathbf{x}_t + \mathbf{r}_t, \quad (2)$$

where $\mathbf{y}_t \in \mathbb{R}^m$ denotes the recorder scalp potentials at time step t, $L \in \mathbb{R}^{m \times n}$ is the FEM lead field matrix, $\mathbf{x}_t \in \mathbb{R}^n$ is called *reconstruction* that gives the coefficients for the basis function representation of the discretized primary current field,

and $\mathbf{r}_t \in \mathbb{R}^m$ denotes the measurement noise that is assumed to follow a zero-mean Gaussian distribution $\mathcal{N}(\mathbf{0}, R_t)$, where R_t is the time-varying covariance matrix.

B. Bayesian MNE and sLORETA

Minimum norm estimate (MNE) [17] can be interpreted within the Bayesian framework when one introduces the measurement noise covariance matrix R and prior covariance matrix P instead of a regularization term [29]. The posterior distribution of Bayesian MNE will follow the Gaussian since the maximum of the distribution

$$\begin{aligned} p(\mathbf{x} \mid \mathbf{y}) \propto\ &\exp\left(-\frac{1}{2}(\mathbf{y} - L\mathbf{x})^{\mathrm{T}} R^{-1}(\mathbf{y} - L\mathbf{x})\right) \\ &\times \exp\left(-\frac{1}{2}\mathbf{x}^{\mathrm{T}} P^{-1}\mathbf{x}\right) \end{aligned} \quad (3)$$

with respect to the brain activity reconstruction $\mathbf{x}$ will constitute the solution that is equivalent to MNE. This so-called maximum a posteriori (MAP) estimate can be also viewed as Gaussian distributed in the frequentist sense:

$$\hat{\mathbf{x}} \sim \mathcal{N}\left(\mathbf{0}, PL^{\mathrm{T}}(LPL^{\mathrm{T}} + R)^{-1}LP^{\mathrm{T}}\right), \quad (4)$$

where the source activity is considered fixed, whereas the observations are random. The derivation of the distribution above is given in Appendix I. The aim of standardization is to equalize the variability of $\hat{\mathbf{x}}$ components corresponding to each source location so that no particular source location is favoured [20], which is achieved by post-hoc weighting the MAP estimate. Additionally, Pascual-Marqui states in the Generalization section in [18] that the standardization can be taken only from a reconstruction vector whose components are uncorrelated and standardized, in the Gaussian sense with respect to the prior. Thereby, the outcome of the matrix product $LP^{1/2}$ is considered as the lead field operator in point spread function-based derivation. We denote the corresponding random variable as $\hat{\boldsymbol{\mu}} := P^{-1/2}\hat{\mathbf{x}}$.

This way the current power estimation, denoted here as the inner product of sLORETA reconstruction $\hat{\mathbf{z}}$ with itself at d-dimensional index set I, reads

$$\begin{aligned} \langle \hat{\mathbf{z}}_I, \hat{\mathbf{z}}_I \rangle &= \langle \hat{\mathbf{x}}_I, \hat{\mathbf{x}}_I \rangle_{\mathrm{sLORETA}} \\ &= \hat{\boldsymbol{\mu}}_I^{\mathrm{T}} \left[\left(P^{1/2}L^{\mathrm{T}}(LPL^{\mathrm{T}} + R)^{-1}LP^{1/2}\right)\right]_{II}^{-1} \hat{\boldsymbol{\mu}}_I, \end{aligned} \quad (5)$$

where the dimension d indicates the degree of orientational freedom of a dipole. One can now see that the standardization as post-hoc weighting is analogical with location-wise standardization of MAP interpreted as a Gaussian random variable for which $\langle \cdot, \cdot \rangle_{\mathrm{sLORETA}}$ induces a Mahalanobis distance [30].

C. Standardized Kalman Filter

The standardization given in (5) can be interpreted as a block-diagonal matrix, which can be decomposed into two symmetric matrices by matrix square root. Due to the symmetry of this sLORETA weighting matrix and the square root of a prior covariance matrix, there is a linear transformation between any Gaussian distributed reconstruction and its
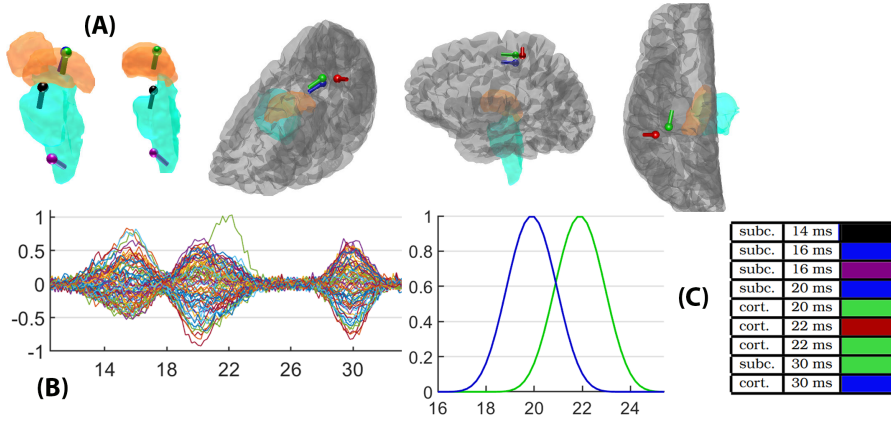
Fig. 1. **(A)** shows the dipole components used in generating synthetic media nerve SEP data. The black marker in pons represents the originator of the P14 component (positive pole of the 14 ms post-stimulus response); the purple one corresponds to the subcortical P16 component; the green marker in the central sulcus (Brodmann area 3b) and the blue one in ventral posterolateral (VPL) thalamus show the cortical and subcortical originator of P20/N20 component (positive/negative pole of the 20 ms post-stimulus response), respectively; green marker in the central sulcus together with the red one in the postcentral gyrus (Brodmann area 1) illustrate two cortical originators of P22/N22. The green marker in the VPL thalamus and the blue one in the central sulcus illustrate the thalamo-cortical originator pair of P30/N30. **(B)** is the EEG recordings produced by the components when 25 dB noise is applied. **(C)** presents the time-evolution and overlap of thalamic (blue) and cortical sulcal (green) source maximized at 20 and 22 ms, respectively, and together constituting the source configuration of simulation I.

standardized counterpart. This includes the dynamic model, i.e., the evolution model and the Gaussian initial state, of the Kalman filter. Moreover, as we show in the Appendix II, linear and bijective (invertible) time-depend transformation of the dynamic model of states leads to a similarly transformed posterior state. Here we define the dynamical standardization matrix W_t at time step t for the MAP estimate of Kalman filter given the states up to $t-1$ following the reasoning in section II-B. This leads to the following formulation of the block-diagonal elements of the weighting matrix

$$[W_t]_{II} = \left[P_{t|t-1}^{-1/2} K_t S_t K_t^{\mathrm{T}} P_{t|t-1}^{-1/2} \right]_{II}^{-1/2}, \quad (6)$$

where $P_{t|t-1}$ is the predicted *a priori* covariance matrix and $P_{t|t}$ is the posterior covariance matrix of Kalman filter. The auxiliary matrices are $S_t = L P_{t|t-1} L^{\mathrm{T}} + R_t$ and $K_t = P_{t|t-1} L^{\mathrm{T}} S_t^{-1}$. With the over-carried transformation of the posterior state and the dynamical standardization matrix, there is the following connection between standardized and regular posteriors

$$\mathcal{N}(\mathbf{z}_t, \hat{P}_{t|t}) = \mathcal{N}\left(W_t P_{t|t-1}^{-1/2} \mathbf{x}_t, W_t P_{t|t-1}^{-1/2} P_{t|t} P_{t|t-1}^{-1/2} W_t^{\mathrm{T}} \right). \quad (7)$$

A concrete benefit from the presented identity is that the standardization weighting can be applied at the end of each update step, thereby, decreasing the computational burden we would otherwise have in the transformation of the model and auxiliary matrices of the algorithm. The full algorithm is presented in Appendix III.

III. EXPERIMENTS

A. MRI-based Segmentation and Source Space for the Head Model

We modeled the head as an 18-compartment volume conductor constructed using openly available T1-weighted MRI data from a healthy subject. The tissue conductivities were set,

i.e., 0.14, 0.33, 0.0064, 1.79, 0.33 and 0.33 S/m for the white and grey matter, skull, cerebrospinal fluid (CSF), sub-cortical structures, and skin, respectively, based on the studies of Dannhauer *et al.* [31] and Shahid *et al.* [32]. Of the remaining compartments, sub-cortical nuclei were associated with the conductivity of the grey matter and the ventricles with that of CSF according to e.g. [27] and the citations therewithin. The tissue compartments were segmented via FreeSurfer software[1]. The head model within 1 mm resolution and the finite element method (FEM) based forward solution were obtained using Matlab-based Zeffiro Interface toolbox [33]. The source space of the forward model contains 10,000 source locations which, for example, is Brainstorm software package's standard source count[2]

B. Media Nerve SEP Simulations

We developed simulated EEG recordings of media nerve SEP data using 9 dipolar originators based on their description given in the literature to validate our approach. We modeled the time interval of 14–30 ms post-stimulus, where the first three components (P14 and P16) are sub-cortical located in the brainstem and thalamus following P20/N20, P22/N22 and P30/N30 components with simultaneous cortical and sub-cortical neural activity.

The SEP activity follows the medial lemniscus pathway and travels to thalamocortical volley [34] which starts from the dorsal column and eventually reaches the somatosensory cortex (SI) [26] where the first cortical responses are expected to be detected. The earliest component P14 is expected to originate from the medial lemniscus [34]. Based on the findings of Buchner *et al.* [35], P16 dipoles are placed in the ventral thalamus [35] and the lower part of the brainstem [36]. The P20/N20 component occurring at 20 ms is modeled by

two dipoles, one placed at Brodmann area 3b and another in the thalamus. Götz *et al.* have found simultaneous subcortical activity, particularly at ventral posterolateral (VPL) thalamus [37] suggesting that the thalamus can be active at the same time in this phase [38]. The peak of the 22 ms component is located either in Brodmann area 1 or 4 [26] from which we have chosen the first one. Similarly to the 20 ms events, the thalamus has been found to be active during the maximum peak of the P22/N22 [39]. At 30 ms, the peak of the cortical generator is placed in the frontal lobe, and the sub-cortical dipole at the ventral thalamus [40].

The exact dipole locations and orientations are presented in Figure 1. The amplitude of dipolar activities are all set to be equally 10 nA m as suggested for a simulation [41], [42]. The time evolution of each component is modeled as a Gaussian pulse with 7 ms duration. We apply a 5 kHz sampling rate in the data generation.

In the simulations, we compare the performance of the Kalman filter (KF), standardized Kalman filter (SKF), and sLORETA to cover the effect of dynamical filtering and the standardization.

In simulation (**I**) we are focusing on the trackability and smoothness of the reconstructed time evolution of the overlapping pair of thalamic and cortical sulcal sources occurring at 20 and 22 ms, respectively, to investigate the dependence of cortical and deep activity in reconstructions presented in the Figure 1(C). Ideally, the pulses should be recovered as independent tracks. The simulation is performed using signal-to-noise ratios (SNR) of 25, 15, and 5 dB that are chosen to be particularly low to highlight the differences. For each noise level, 50 samples of measurement data were gathered and then reconstructed. The results are displayed as time-depend curves of averaged activity that are normalized by the maximum value obtained at 25 dB.

In the follow-up simulation (**II**), we reconstruct the whole time series of 9 sources and display the reconstructions of the component originators at their peaks, where SNR is the highest. The data was created using 25 dB SNR. The simulated EEG recordings are presented in Figure 1(B).

C. Experiment Using Real SEP Data

The dataset used in the experiment was obtained from 49 years old right-handed male. The subject had no history of psychiatric or neurological disorders and had given written informed consent before the experiment. The institution's ethical review board (Ethik Kommission der Ärztekammer Westfalen–Lippe und der WWU) approved all experimental procedures on 02.02.2018 (Ref. No. 2014-156-f-S). The dataset contains defaced head model and montage-averaged EEG recordings. MRI dataset, from which the head model was constructed, was measured by MAGNETOM Prisma scanner 3.0 T (Release D13, Siemens Medical Solutions, Erlangen, Germany) with T1-weighting (T1W) fast gradient-echo pulse sequence. SEP measurements were performed using 80 AgCl sintered ring electrodes (EASYCAP GmbH, Herrsching, Germany) with 74 EEG channels in the 10–10 system. A notch filter was applied in order to remove the interference caused

by harmonics of the 50 Hz power line frequency and the 60 Hz of the monitor from which the subject watched a video during the measurement as a means to increase their attention. A total of 1200 stimuli were recorded for averaging, following the guidelines for spinal and subcortical SEPs [43]. We are obtaining the reconstructions at the time spots of the major SEP components, the activity corresponding to the 14-30 ms post-stimulus peaks P14, P16, P20/N20, P22/N22, and P30/N30 similar to the simulated experiment described in the previous section III-B. The dataset is openly available [44].

D. Model Parameter Selections

In this study, we use a simple random walk of the reconstruction as the evolution model of KF that reads

$$\mathbf{x}_t = \mathbf{x}_{t-1} + \mathbf{q}_t, \tag{8}$$

where $\mathbf{q}_t$ obeys Gaussian $\mathcal{N}(\mathbf{0}, Q_t)$. In practice, we let the current density change in Gaussian distributed increments over time at every calculation node of the head model. To select the initial prior covariance, we use the prior estimation method based on the concept of total variation over the present head model [45], where the activity on individual source locations are assumed to be identically distributed and independent. Thus, the evolution covariance matrix is a diagonal matrix with equal variances θ. Prior covariance is initialized equally for both Kalman filter implementations to ensure a fair comparison. Applying the same technique to evolution prior, the evolution is set to be identically and independently distributed with variances q. Assuming that the expected $L2$-norm of activity change is equal in every source location, we get the estimation for evolution variance

$$q = \sigma_1(L)^2 \, 10^{-\rho/20} \theta / f, \tag{9}$$

where $\sigma_1(L)$ denotes the largest singular value of the lead field, f is the sampling frequency of the measurements, and ρ is a free parameter relating prior variance and evolution of prior variance in decibels. The value was set to be 34 dB by estimating the variance of the change rate of MNE and sLORETA reconstructions.

IV. RESULTS

A. Media Nerve SEP Simulations

The results of simulation (**I**), concerning the temporally overlapping thalamo-cortical pair of sources at 20 and 22 ms, show an inability to detect the deep source while using the basic implementation of Kalman as seen in the blue deep activity strength curve that over time stays zero during the whole time series on the first row of Figure 2 for each noise level case 25, 15, and 5 dB from left to right, respectively. On one hand, the Kalman filter tracks the beginning of the cortical activity (green curve) with only slight deviations on the postcentral gyrus at 25 dB (the first on the left in the figure) as the lighter coloring represents the standard deviation of activity tracks at each time point. On the other hand, the damping of the activity is slower than it should be as we can see comparing the track to Figure 1(C). sLORETA is able to
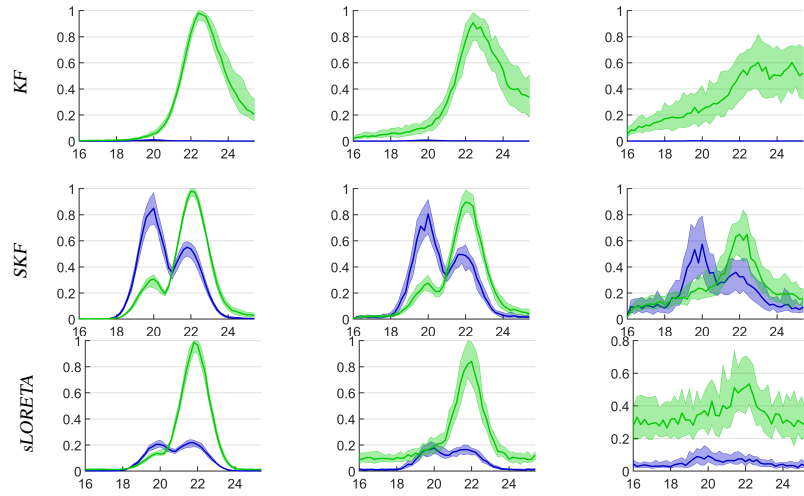
Fig. 2. Mean and the standard deviation of tracked brain activity time evolutions of deep (blue) and cortical (green) components in simulation (**I**) under different noise levels (25, 15, 5 dB from left to right). The area covered in a lighter coloring represents the standard deviation over samples and the darker green curve represents the sample mean. The data contains 50 noise realizations.
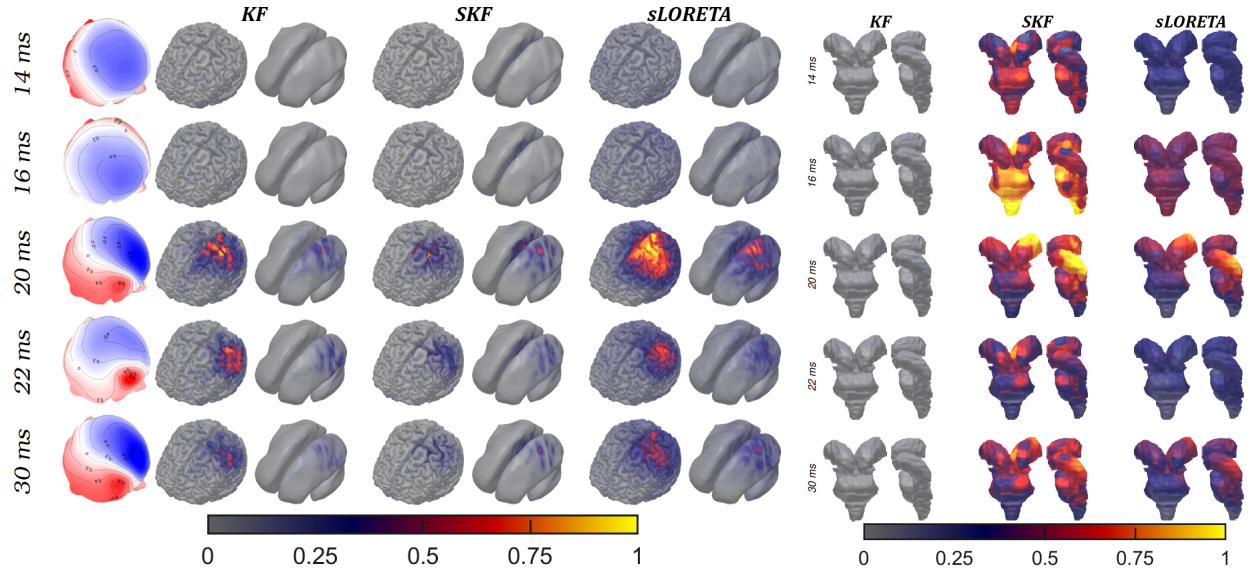

Fig. 3. **Left:** Topographic plots and cortical part of the reconstructions on peak time points of simulated SEP data for all three methods. Reconstructions are scaled from 0 to 1 normalizing by the highest reconstruction magnitude over the whole time series. **Right:** Sub-cortical part of the reconstructions on thalamus and brainstem.

detect both sources with only minor deviations at 15 and 25 dB. However, the strength of deep activity is suppressed and non-independent. In an independent scenario, the estimated strength of the peaked deep activity would be equal to the cortical activity, and we would not see increased activity on the thalamus when cortical activity appears. In the case of Kalman coupled with the standardization, we obtain the highest activity strength on the deep structure among the compared methods. Also with SKF, small deviations can be observed in the results of 15 and 25 dB.

In simulation (**II**), presented in Figures 3, all reconstructions display the cortical activity at the correct location for tangential sources at 20 and 30 ms. The basic Kalman slightly mislocalizes the radially oriented gyral source at 22 ms. Subcortical sources at 14 and 16 ms produce a faint cortical projection for sLORETA, which yielded overall less focal results than with filtering approaches while SKF was the most

focal. While KF does not detect any activity in deep structures, its standardized counterpart localizes the activities correctly in the medulla-pontine junction at 14 ms, the bottom of the brainstem at 16 ms, and in left thalamus at 20, 22, and 30 ms.

B. Experiment With Real SEP Data

In Figure 4, for SKF and sLORETA, the reconstruction peak on the brainstem is located at pons for the 14 ms component and at the bottom of the brainstem at 16 ms. In line with the simulations, deep activities are not detected by KF. In addition, KF localizes the cortical activity to the superior parietal lobule while SKF and sLORETA have the cortical maximum on the central sulcus at 20, 22, and 30 ms. Of the two, SKF has a slightly more focal reconstruction, i.e., a smaller spread of activity distribution. Reconstruction maxima of the thalamic component of P20/N20 are obtained on the
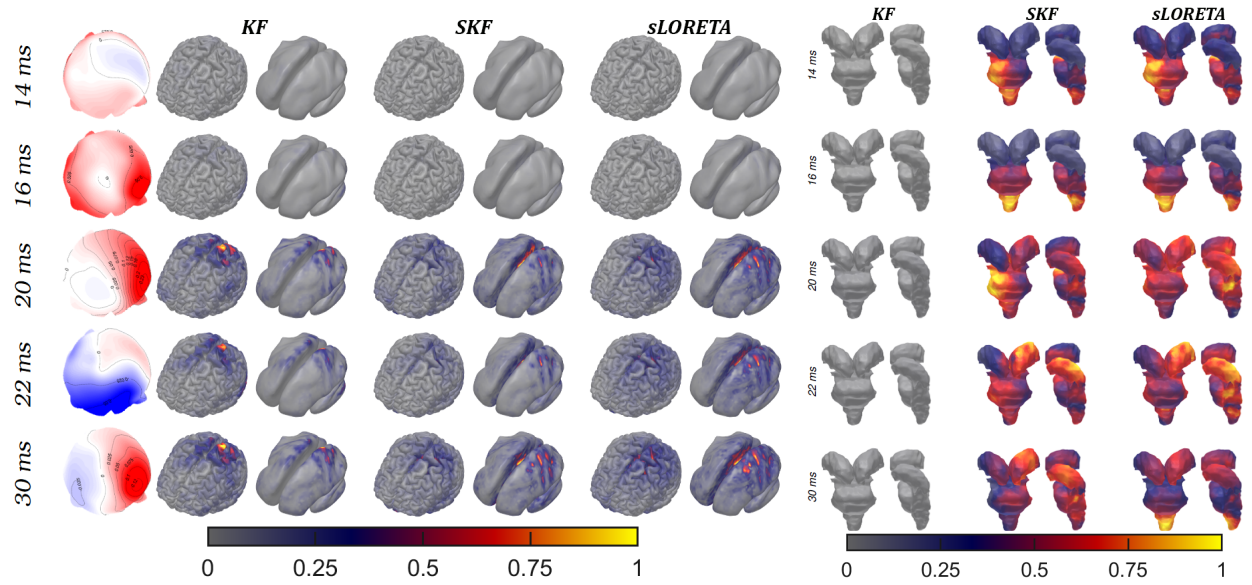
Fig. 4. **Left:** Topographic plots and cortical part of the reconstructions obtained from real SEP peak time points for all three methods. **Right:** Sub-cortical part of the reconstructions on thalamus and brainstem.

brainstem in a different location with SKF than sLORETA. Both of the reconstruction peaks extend to the left thalamus. The reconstructions of subcortical activity at 22 ms found via SKF and sLORETA are similar, and their maxima locate at the left thalamus. A small discrepancy can again be observed in SKF and sLORETA reconstructions of the subcortical activity at 30 ms as the SKF peak is located at the left thalamus and the peak of sLORETA is at the bottom of the brainstem.

V. DISCUSSION AND CONCLUSIONS

In this paper, we have introduced a way to couple the standardization of sLORETA with the Kalman filter in a mathematically rigorous manner. Our formulation allows the utilization of the entire source space without the use of the nearest neighborhood space reduction [13], [16], simplified mesh [11], or rank-reduced model [5], and of a common fine spatial resolution, e.g., a space of 10.000 sources, without the need for high-performance computing [14]. Based on the two numerical simulations considering the traceability of time evolution and localizability of activity peaks of synthetic median nerve SEP originators., in comparison to sLORETA and Kalman filter (KF), the standardized Kalman filter (SKF) inherits the advantages of both methods while seeming to provide a greater focality of the reconstruction as its own ability. The results show how the KF without any aid cannot recover deep activity from EEG recordings. This is no surprise since KF is closely related to MNE which is notorious for its ineptitude to recover far-field sources. The low-resolution aspect of sLORETA manifested itself in reconstructions of deep activities: other than reconstruction of 20 ms are so widespread that the activity is hard to be localized in sub-levels of thalamus and brainstem. As is the case with the standardized MNE (sLORETA), standardization makes the subcortical activity detectable with the Kalman filter. Also, robustness to measurement noise obtained with standardization in earlier studies [21], [22] and in our simulation (**I**)

considering trackability, is present with SKF as only slight deviations are obtainable. Moreover, the benefits of dynamical modeling can be seen when comparing the track of SKF to sLORETA's ones: SKF is the only method compared that is able to retain the time evolution of subcortical and cortical activity at 5 dB. Reconstructions obtained with real SEP data seem clearer compared to the simulated cases which may be due to a high number of averaged montages in real data compared to 25 dB noise used in the simulated simulation (**II**). Locations of cortical and subcortical peaks of sLORETA and SKF are mostly according to the literature reviewed in the section III-B, but 22 ms cortical peak at the central sulcus and extending over its walls is inconclusive due to the given options of Brodmann areas 2 and 4. Interestingly, the basic Kalman filter mislocalizes the cortical activity. A probable explanation could be that the earlier subcortical components get reconstructed evenly on the cortex because of KF's depth bias which interferes with the estimation of cortical dynamics causing false localization. At 20 ms, the subcortical reconstruction of SKF and sLORETA are partly spread over the VPL thalamus, peaking in different parts of the brainstem. The deviated peaks, as compared to the expected thalamic activity, might follow from the given prior, which affects the reconstruction in weakly distinguishable areas. due to the standardization, SKF and sLORETA might have slightly exaggerated the depth of the gyral 22 ms originator, which is present in each reconstruction found in the simulated experiment (**II**). With 30 ms SKF's peak is located in agreement with the literature as the sLORETA peak is at the bottom of the brainstem.

A lot of the estimation power of the Kalman filter comes from the carefully selected evolution model, which is yet to be unlocked since we used the random walk which is the simplest model assumption after static dipoles in this study. A proper evolution model could resolve some of the issues raised from the results, e.g., slight non-independency of cortical

and sub-cortical activities and too slowly vanishing activities. However, even with this simple evolution model, the results are encouraging for further experiments and the development of evolution models tailored to neural imaging. Due to the focality and high noise robustness of SKF, the applicability of the method to recover epileptic sources could be investigated as a potential future work.

APPENDIX I
DISTRIBUTION OF MAXIMUM A POSTERIORI ESTIMATES IN THE CASE OF A GAUSSIAN POSTERIOR

Let us consider the following marginal likelihood constituting from a Gaussian measurement noise $\mathbf{r} \sim \mathcal{N}(\mathbf{0}, R)$ and prior $\mathbf{x} \sim \mathcal{N}(\mathbf{0}, P)$, stating

$$p\left(L\mathbf{x} + \mathbf{r}\right) = \int_{\Omega} p(L\mathbf{x} + \mathbf{r} \mid \mathbf{x})p(\mathbf{x})\, \mathrm{d}\mathbf{x} = \mathcal{N}(\mathbf{0}, LPL^T + R). \tag{10}$$

By taking advantage of the linearity of MNE estimation with respect to the measurement data, we obtain the distribution for *maximum a posteriori* estimate as

$$\hat{\mathbf{x}} = PL^T(LPL^T + R)^{-1}(L\mathbf{x} + \mathbf{r}) \\ \sim \mathcal{N}\left(\mathbf{0}, PL^{\mathrm{T}}(LPL^{\mathrm{T}} + R)^{-1}LP\right) \tag{11}$$

noting that covariance matrices are symmetric, i.e., $P^{\mathrm{T}} = P$.

APPENDIX II
LINEAR TRANSFORMATION ON KALMAN FILTER'S ESTIMATION

In the case of a time-depend linear and bijective transformation of the state vector $\mathbf{z}_t = M_t\mathbf{x}_t$, the dynamical model should be written as

$$\mathbf{z}_t = M_t(A_t\mathbf{x}_{t-1} + \mathbf{q}_t) = M_tA_tM_{t-1}^{-1}\mathbf{z}_{t-1} + M_t\mathbf{q}_t. \tag{12}$$

When the prior is distributed as $\mathbf{x}_t \mid \mathbf{y}_{1:t-1} \sim \mathcal{N}(A_t\mathbf{x}_{t-1|t-1}, P_{t|t-1})$, we get

$$\mathbf{z}_t \mid \mathbf{y}_{1:t-1} \sim \mathcal{N}\left(M_tA_t\mathbf{x}_{t-1|t-1}, M_tP_{t|t-1}M_t^{\mathrm{T}}\right) \tag{13}$$

by the linear transformation property of Gaussian distributions. Using the distribution above, we can write the joint distribution

$$\begin{bmatrix} \mathbf{z}_t \\ \mathbf{y}_t \end{bmatrix} \sim \mathcal{N}\left(\begin{bmatrix} \mathbf{z}_{t|t-1} \\ LW_t^{-1}\mathbf{z}_{t|t-1} \end{bmatrix}, \Sigma\right), \tag{14}$$

where

$$\Sigma = \begin{bmatrix} M_tP_{t|t-1}M_t^{\mathrm{T}} & M_tP_{t|t-1}L^{\mathrm{T}} \\ LP_{t|t-1}M_t^{\mathrm{T}} & LP_{t|t-1}L^{\mathrm{T}} + R \end{bmatrix}. \tag{15}$$

Next, using the Bayesian rule, we obtain

$$p(\mathbf{z}_t \mid \mathbf{y}_t) = \frac{p(\mathbf{y}_t \mid \mathbf{z}_t)p(\mathbf{z}_t \mid \mathbf{y}_{1:t-1})}{p(\mathbf{y}_t)} \tag{16}$$

$$= \mathcal{N}\left(\mathbf{z}_{t|t}, M_tP_{t|t}M_t^{\mathrm{T}}\right),$$

where

$$\mathbf{z}_{t|t} = \mathbf{z}_{t|t-1} + M_tK_t(\mathbf{y}_t - LM_t^{-1}\mathbf{z}_{t|t-1}) \tag{17}$$

and

$$M_tP_{t|t}M_t^{\mathrm{T}} = M_tP_{t|t-1}M_t^{\mathrm{T}} - M_tK_tS_tK_t^{\mathrm{T}}M_t^{\mathrm{T}}, \tag{18}$$

while

$$p(\mathbf{x}_t \mid \mathbf{y}_t) = \mathcal{N}\left(\mathbf{x}_{t|t-1} + K_t(\mathbf{y}_t - L\mathbf{x}_{t|t-1}), P_{t|t}\right). \tag{19}$$

Now we can see that the linear transformation M_t has carried from the prior estimate to the posterior state, i.e., $\mathbf{z}_t \mid \mathbf{y}_t = M_t\mathbf{x}_t \mid \mathbf{y}_t$ for all $t = 1, \cdots, T$.

APPENDIX III
STANDARDIZED KALMAN FILTER ALGORITHM

Considering the typical measurement model of brain imaging and a general linear dynamical model

$$\mathbf{y}_t = L\mathbf{x}_t + \mathbf{r}_t, \tag{20}$$
$$\mathbf{x}_t = A_t\mathbf{x}_{t-1} + \mathbf{q}_t, \tag{21}$$

where $\mathbf{r}_t \sim \mathcal{N}(\mathbf{0}, R_t)$ and $\mathbf{q}_t \sim \mathcal{N}(\mathbf{0}, Q_t)$. Now the prediction step is executed as the following

$$\mathbf{x}_{t|t-1} = A_t\mathbf{x}_{t-1|t-1}$$
$$P_{t|t-1} = A_tP_{t-1|t-1}A_t^{\mathrm{T}} + Q_t$$

and the update step reads as

$$S_t = LP_{t|t-1}L^{\mathrm{T}} + R_t$$
$$K_t = P_{t|t-1}L^{\mathrm{T}}S_t^{-1}$$
$$\mathbf{x}_{t|t} = \mathbf{x}_{t|t-1} + K_t\left(\mathbf{y}_t - L\mathbf{x}_{t|t-1}\right)$$
$$P_{t|t} = P_{t|t-1} - K_tS_tK_t^{\mathrm{T}}$$
$$[W_t]_{II} = \left[P_{t|t-1}^{-1/2}K_tS_tK_t^{\mathrm{T}}P_{t|t-1}^{-1/2}\right]_{II}^{-1/2}$$
$$\mathbf{z}_{t|t} = W_tP_{t|t-1}^{-1/2}\mathbf{x}_{t|t}.$$

The second last step introduces the time-depend post-hoc weights as a block diagonal matrix, where each block is $d \times d$ matrix and d is the degree of orientational freedom of the dipole vector. Vector $\mathbf{z}_{t|t}$ gives the standardized Kalman estimation at time step t. Estimation is obtained first by normalizing $\mathbf{x}_{t|t}$ with respect to prior and then by taking the standardization W_t as the procedure is described in [18] for independent sources.

REFERENCES

[1] B. He, A. Sohrabpour, E. Brown, and Z. Liu, "Electrophysiological source imaging: A noninvasive window to brain dynamics," *Annual review of biomedical engineering*, vol. 20, no. 1, pp. 171–196, 2018.

[2] C. M. Michel, M. M. Murray, G. Lantz, S. Gonzalez, L. Spinelli, and R. Grave de Peralta, "EEG source imaging," *Clinical Neurophysiology*, vol. 115, no. 10, pp. 2195–2222, 2004.

[3] C. Kaur, P. Singh, A. Bisht, G. Joshi, and S. Agrawal, "Recent developments in spatio-temporal EEG source reconstruction techniques," *Wireless personal communications*, vol. 122, no. 2, pp. 1531–1558, 2022.

[4] N. J. Trujillo-Barreto, E. Aubert-Vázquez, and W. D. Penny, "Bayesian M/EEG source reconstruction with spatio-temporal priors," *NeuroImage (Orlando, Fla.)*, vol. 39, no. 1, pp. 318–335, 2008.

[5] W. Ou, M. S. Hämäläinen, and P. Golland, "A distributed spatio-temporal EEG/MEG inverse solver," *NeuroImage (Orlando, Fla.)*, vol. 44, no. 3, pp. 932–946, 2009.

[6] M. Dannhauer, E. Lämmel, C. H. Wolters, and T. R. Knösche, "Spatio-temporal regularization in linear distributed source reconstruction from EEG/MEG: A critical evaluation," *Brain topography*, vol. 26, no. 2, pp. 229–246, 2013.

[7] D. Paz-Linares, M. Vega-Hernández, P. A. Rojas-López, P. A. Valdés-Hernández, E. Martínez-Montes, and P. A. Valdés-Sosa, "Spatio temporal EEG source imaging with the hierarchical Bayesian elastic net and elitist Lasso models," *Frontiers in neuroscience*, vol. 11, pp. 635–635, 2017.

[8] S. Cui *et al.*, "EEG source localization using spatio-temporal neural network," *China communications*, vol. 16, no. 7, pp. 131–143, 2019.

[9] M. Rullmann, A. Anwander, M. Dannhauer, S. K. Warfield, F. H. Duffy, and C. H. Wolters, "EEG source analysis of epileptiform activity using a 1 mm anisotropic hexahedra finite element head model," *NeuroImage*, vol. 44, no. 2, pp. 399–410, 2009.

[10] R. E. Kalman and R. S. Bucy, "New results in linear filtering and prediction theory," *Journal of basic engineering*, vol. 83, no. 1, pp. 95–108, 1961.

[11] A. Galka, O. Yamashita, T. Ozaki, R. Biscay, and P. Valdés-Sosa, "A solution to the dynamical inverse problem of EEG generation using spatiotemporal Kalman filtering," *NeuroImage (Orlando, Fla.)*, vol. 23, no. 2, pp. 435–453, 2004.

[12] M. J. Barton *et al.*, "Evaluating the performance of Kalman-filter-based EEG source localization," *IEEE transactions on biomedical engineering*, vol. 56, no. 1, pp. 122–136, 2009.

[13] O. Yamashita, A. Galka, T. Ozaki, R. Biscay, and P. Valdes-Sosa, "Recursive penalized least squares solution for dynamical inverse problems of EEG generation," *Human brain mapping*, vol. 21, no. 4, pp. 221–235, 2004.

[14] C. J. Long, P. L. Purdon, S. Temereanca, N. U. Desai, M. S. Hämäläinen, and E. N. Brown, "State-space solutions to the dynamic magnetoencephalography inverse problem using high performance computing," *The annals of applied statistics*, vol. 5, no. 2B, pp. 1207–1228, 2011.

[15] L. Hamid, U. Aydin, C. Wolters, U. Stephani, M. Siniatchkin, and A. Galka, "MEG-EEG fusion by Kalman filtering within a source analysis framework," in *2013 35th Annual International Conference of the IEEE Engineering in Medicine and Biology Society (EMBC)*, vol. 2013. United States: IEEE, 2013, pp. 4819–4822.

[16] L. Hamid *et al.*, "Source imaging of deep-brain activity using the regional spatiotemporal Kalman filter," *Computer Methods and Programs in Biomedicine*, vol. 200, p. 105830, 2021.

[17] M. Hämäläinen and R. Ilmoniemi, "Interpreting magnetic fields on the brain: minimum norm estimates," *Medical & biological engineering & computing*, vol. 32, no. 1, pp. 35–42, 1994.

[18] R. D. Pascual-Marqui, "Standardized low-resolution brain electromagnetic tomography (sLORETA): technical details." *Methods and findings in experimental and clinical pharmacology*, vol. 24, pp. 5–12, 2002.

[19] K. Sekihara, M. Sahani, and S. S. Nagarajan, "Localization bias and spatial resolution of adaptive and non-adaptive spatial filters for MEG source reconstruction," *NeuroImage (Orlando, Fla.)*, vol. 25, no. 4, pp. 1056–1067, 2005.

[20] R. D. Pascual-Marqui, "Discrete, 3D distributed, linear imaging methods of electric neuronal activity. Part 1: exact, zero error localization," 2007.

[21] S. Saha, Y. I. Nesterets, M. Tahtali, and T. E. Gureyev, "Evaluation of spatial resolution and noise sensitivity of sLORETA method for EEG source localization using low-density headsets," *Biomedical physics & engineering express*, vol. 1, no. 4, pp. 45 206–, 2015.

[22] M. Dümpelmann, T. Ball, and A. Schulze-Bonhage, "sLORETA allows reliable distributed source reconstruction based on subdural strip and grid recordings," *Human brain mapping*, vol. 33, no. 5, pp. 1172–1188, 2012.

[23] R. G. Emerso and T. A. Pedley, "Generator sources of median somatosensory evoked potentials," *Journal of clinical neurophysiology*, vol. 1, no. 2, pp. 203–218, 1984.

[24] F. Babiloni, C. Babiloni, L. Locche, F. Cincotti, P. M. Rossini, and F. Carducci, "High-resolution electro-encephalogram: source estimates of laplacian-transformed somatosensory-evoked potentials using a realistic subject head model constructed from magnetic resonance images," *Medical & biological engineering & computing*, vol. 38, no. 5, pp. 512–519, 2000.

[25] M. Valeriani, D. Le Pera, D. Niddam, L. Arendt-Nielsen, and A. C. Chen, "Dipolar source modeling of somatosensory evoked potentials to painful and nonpainful median nerve stimulation," *Muscle & nerve*, vol. 23, no. 8, pp. 1194–1203, 2000.

[26] H. Buchner *et al.*, "Somatotopy of human hand somatosensory cortex revealed by dipole source analysis of early somatosensory evoked potentials and 3D-NMR tomography," *Electroencephalography and Clinical Neurophysiology/Evoked Potentials Section*, vol. 96, no. 2, pp. 121–134, 1995.

[27] A. Rezaei *et al.*, "Reconstructing subcortical and cortical somatosensory activity via the RAMUS inverse source analysis technique using median nerve SEP data," *NeuroImage (Orlando, Fla.)*, vol. 245, pp. 118 726–118 726, 2021.

[28] S. Pursiainen, J. Vorwerk, and C. H. Wolters, "Electroencephalography (EEG) forward modeling via H(div) finite element sources with focal interpolation," *Physics in Medicine and Biology*, vol. 61, no. 24, p. 8502, 2016.

[29] D. Wipf and S. Nagarajan, "A unified Bayesian framework for MEG/EEG source imaging," *NeuroImage (Orlando, Fla.)*, vol. 44, no. 3, pp. 947–966, 2009.

[30] P. C. Mahalanobis, "On the generalized distance in statistics," *Proceedings of the National Institute of Sciences (Calcutta)*, vol. 2, pp. 49–55, 1936.

[31] M. Dannhauer, B. Lanfer, C. H. Wolters, and T. R. Knösche, "Modeling of the human skull in EEG source analysis," *Human Brain Mapping*, vol. 32, pp. 1383–1399, 2011.

[32] S. S. Shahid, M. Bikson, H. Salman, P. Wen, and T. Ahfock, "The value and cost of complexity in predictive modelling: role of tissue anisotropic conductivity and fibre tracts in neuromodulation," *Journal of neural engineering*, vol. 11, no. 3, pp. 036 002–19, 2014.

[33] Q. He, A. Rezaei, and S. Pursiainen, "Zeffiro user interface for electromagnetic brain imaging: a GPU accelerated FEM tool for forward and inverse computations in Matlab," *Neuroinformatics*, 10 2019.

[34] P. Noël, I. Ozaki, and J. E. Desmedt, "Origin of N18 and P14 far-fields of median nerve somatosensory evoked potentials studied in patients with a brain-stem lesion," *Electroencephalography and clinical neurophysiology*, vol. 98, no. 2, pp. 167–170, 1996.

[35] H. Buchner, T. D. Waberski, M. Fuchs, H.-A. Wischmann, R. Beckmann, and A. Rienäcker, "Origin of P16 median nerve SEP component identified by dipole source analysis: subthalamic or within the thalamo-cortical radiation?" *Experimental brain research*, vol. 104, no. 3, pp. 511–518, 1995.

[36] C.-L. Hsieh, F. Shima, S. Tobimatsu, S.-J. Sun, and M. Kato, "The interaction of the somatosensory evoked potentials to simultaneous finger stimuli in the human central nervous system. a study using direct recordings," *Electroencephalography and Clinical Neurophysiology/Evoked Potentials Section*, vol. 96, no. 2, pp. 135–142, 1995.

[37] J. Haueisen, L. Leistritz, T. Süsse, G. Curio, and H. Witte, "Identifying mutual information transfer in the brain with differential-algebraic modeling: Evidence for fast oscillatory coupling between cortical somatosensory areas 3b and 1," *NeuroImage*, vol. 37, no. 1, pp. 130–136, 2007.

[38] T. Götz, R. Huonker, O. W. Witte, and J. Haueisen, "Thalamocortical impulse propagation and information transfer in EEG and MEG," *Journal of clinical neurophysiology*, vol. 31, no. 3, pp. 253–260, 2014.

[39] C. Papadelis, S. B. Eickhoff, K. Zilles, and A. A. Ioannides, "BA3b and BA1 activate in a serial fashion after median nerve stimulation: Direct evidence from combining source analysis of evoked fields and cytoarchitectonic probabilistic maps," *NeuroImage (Orlando, Fla.)*, vol. 54, no. 1, pp. 60–73, 2011.

[40] A. M. Cebolla and G. Chéron, "Sensorimotor and cognitive involvement of the beta–gamma oscillation in the frontal n30 component of somatosensory evoked potentials," *Neuropsychologia*, vol. 79, pp. 215–222, 2015.

[41] M. Hämäläinen, R. Hari, R. J. Ilmoniemi, J. Knuutila, and O. V. Lounasmaa, "Magnetoencephalography — theory, instrumentation, and applications to invasive studies of the working human brain," *Reviews of Modern Physics*, vol. 65, pp. 413–498, 1993.

[42] D. M. Goldenholz, S. P. Ahlfors, M. S. Hämäläinen, D. Sharon, M. Ishitobi, L. M. Vaina, and S. M. Stufflebeam, "Mapping the signal-to-noise-ratios of cortical sources in magnetoencephalography and electroencephalography," *Human brain mapping*, vol. 30, no. 4, pp. 1077–1086, 2009.

[43] G. Cruccu *et al.*, "Recommendations for the clinical use of somatosensory-evoked potentials," *Clinical Neurophysiology*, vol. 119, no. 8, pp. 1705–1719, 2008.

[44] M. C. Piastra *et al.*, "The WWU DUNEuro reference data set for combined EEG/MEG source analysis," Jun. 2020, The research related to this dataset was supported by the German Research Foundation (DFG) through project WO1425/7-1 and the EU project ChildBrain (Marie Curie Innovative Training Networks, grant agreement 641652).

[45] A. Rezaei, M. Antonakakis, M. Piastra, C. H. Wolters, and S. Pursiainen, "Parametrizing the conditionally Gaussian prior model for source localization with reference to the P20/N20 component of median nerve SEP/SEF," *Brain sciences*, vol. 10, no. 12, p. 934, 2020.